


Diurnal Variations of the Flux Imbalance Over Homogeneous and Heterogeneous Landscapes

Yanzhao Zhou^{1,2}  · Dan Li³ · Heping Liu⁴ · Xin Li^{5,6}

Received: 11 August 2017 / Accepted: 3 May 2018 / Published online: 17 May 2018
© Springer Science+Business Media B.V., part of Springer Nature 2018

Abstract It is well known that the sum of the turbulent sensible and latent heat fluxes as measured by the eddy-covariance method is systematically lower than the available energy (i.e., the net radiation minus the ground heat flux). We examine the separate and joint effects of diurnal and spatial variations of surface temperature on this flux imbalance in a dry convective boundary layer using the Weather Research and Forecasting model. Results show that, over homogeneous surfaces, the flux due to turbulent-organized structures is responsible for the imbalance, whereas over heterogeneous surfaces, the flux due to mesoscale or secondary circulations is the main contributor to the imbalance. Over homogeneous surfaces, the flux imbalance in free convective conditions exhibits a clear diurnal cycle, showing that the flux-imbalance magnitude slowly decreases during the morning period and rapidly increases during the afternoon period. However, in shear convective conditions, the flux-imbalance magnitude is much smaller, but slightly increases with time. The flux imbalance over heterogeneous surfaces exhibits a diurnal cycle under both free and shear convective conditions, which is similar to that over homogeneous surfaces in free convective conditions, and is also consistent with the general trend in the global observations. The rapid increase in the flux-imbalance magnitude during the afternoon period is mainly caused by the afternoon decay of the turbulent kinetic energy (TKE). Interestingly, over heterogeneous surfaces, the flux imbalance is linearly related to the TKE and the difference between the potential tem-

✉ Xin Li
lixin@lzb.ac.cn

¹ Key Laboratory of Remote Sensing of Gansu Province, Northwest Institute of Eco-Environment and Resources, Chinese Academy of Sciences, Lanzhou, Gansu, China

² University of Chinese Academy of Sciences, Beijing, China

³ Department of Earth and Environment, Boston University, Boston, MA, USA

⁴ Laboratory for Atmospheric Research, Department of Civil and Environmental Engineering, Washington State University, Pullman, WA, USA

⁵ Institute of Tibetan Plateau Research, Chinese Academy of Sciences, Beijing, China

⁶ CAS Center for Excellence in Tibetan Plateau Earth Sciences, Chinese Academy of Sciences, Beijing, China

perature and surface temperature, ΔT ; the larger the TKE and ΔT values, the smaller the flux-imbalance magnitude.

Keywords Convective boundary layer · Diurnal variations · Flux imbalance · Large-eddy simulation · Spatial heterogeneity

1 Introduction

The eddy-covariance method has been one of the most direct and reliable approaches for measuring turbulent exchange between the biosphere and the atmosphere, with currently more than 900 active eddy-covariance sites around the world (<https://fluxnet.fluxdata.org/sites/site-summary/>). One common issue across these eddy-covariance sites is that the sum of sensible and latent heat fluxes is smaller than the difference between the net radiation and ground heat flux by as much as 30% (Twine et al. 2000; Wilson et al. 2002; Oncley et al. 2007; Foken 2008; Aubinet et al. 2012; Xu et al. 2017). The surface energy imbalance or non-closure problem has been the subject of active research in recent years. Potential causes, including mismatches in the footprints of radiation and turbulent-flux measurements, measurement/computational errors, a significant advective flux, and inadequate sampling of large-scale turbulent eddies (e.g., the time scale of eddies > 30 min), have been discussed and reviewed elsewhere (Mahrt 1998, 2010; Twine et al. 2000; Foken et al. 2006, 2011; Foken 2008; Wang et al. 2009; Leuning et al. 2012; Wohlfahrt and Widmoser 2013). Among these potential causes, the inadequate sampling of large-scale turbulent eddies has been increasingly acknowledged as one of the leading contributors to the surface energy imbalance (Gao et al. 2010, 2017; Foken et al. 2011; Stoy et al. 2013). For example, using surface observations (e.g., lidar and tower measurements) and large-eddy simulations (LES), Eder et al. (2015a, b) found that large eddies with time scales > 30 min induced by secondary circulations are the major cause for the energy imbalance at their sites. Gao et al. (2017) discovered that the enlarged phase difference between the vertical velocity component and the water vapour density associated with large eddies leads to an increased energy imbalance.

As an important numerical tool in studying the atmospheric boundary layer (ABL), LES has recently been applied to investigate the flux-imbalance problem. For example, Kanda et al. (2004) (hereafter K04) used virtual towers in their LES investigation to mimic eddy-covariance observations in a convective boundary layer (CBL), and found that turbulent-organized structures with time scales much longer than those of thermal plumes are responsible for the flux imbalance over homogenous surfaces. Based on their definition, turbulent-organized structures only refer to large coherent eddies, but not secondary circulations caused by, for example, surface heterogeneity. Later, with a much finer spatial resolution, Steinfeld et al. (2007) (hereafter S07) investigated the effect of stable stratification on the flux imbalance. Huang et al. (2008) (hereafter H08) decomposed the flux imbalance into bottom-up and top-down components, and further conceptualized the imbalance as a function of non-dimensionalized parameters related to turbulent velocity scales and source locations. Recently, Schalkwijk et al. (2016) (hereafter S16) conducted continuous year-long LES integrations forced by measured atmospheric variables to study the flux imbalance at the Cabauw site in the Netherlands. While these LES studies focused on homogeneous surfaces, there are also LES studies that investigate the flux imbalance over heterogeneous surfaces. For example, Inagaki et al. (2006) (hereafter I06) analyzed the effect of a one-dimensional sinusoidal variation of surface heat flux on the flux imbalance, and found that mesoscale or

secondary circulations have a larger impact on the flux imbalance than turbulent-organized structures. Using a control-volume approach (Finnigan et al. 2003), Eder et al. (2015b) (hereafter E15) found that secondary circulations are responsible for the underestimation of turbulent fluxes in a forest–desert setting. Recently, De Roo and Mauder (2017) also used the control-volume method to analyze the effect of heterogeneity length scales on the flux imbalance under free convective conditions, and found a correlation between the flux imbalance and the difference between the sonic temperature and surface temperature.

Most of the aforementioned LES studies were designed to investigate the flux imbalance in the quasi-steady state. Although S16 conducted year-long integrations, due to the diurnal variation of other environmental factors, it is difficult to analyze the effects of a diurnally-varying surface heat flux on the flux imbalance in S16. Therefore, the fundamental question of how the flux imbalance is influenced by the diurnal cycle of surface temperature over homogeneous and heterogeneous surfaces has not been investigated. In this study, we aim to quantify the separate and joint effects of diurnal variation and spatial heterogeneity of surface temperature on the flux imbalance.

2 Method

2.1 Flux Imbalance Over Homogeneous Surfaces

As the theoretical background of computing the flux imbalance over a homogeneous surface using LES results is well documented in K04 and S07, only a brief description is provided here. In the following, we consider a variable φ with the spatial mean (averaged over both x and y directions in a horizontal plane) as $[\varphi]$ and the temporal mean as $\bar{\varphi}$; fluctuations from the spatial and temporal mean values are denoted as φ'' and φ' , respectively. The instantaneous vertical kinematic heat flux F is

$$F(x, y, z, t) = w\theta, \tag{1}$$

where w and θ indicate the vertical velocity component and potential temperature, respectively. According to Reynolds decomposition, the temporally- and spatially-averaged vertical kinematic heat fluxes can be written as

$$\bar{F}(x, y, z) = \bar{w}\bar{\theta} + \overline{w'\theta'}, \tag{2}$$

$$[F](z, t) = [w][\theta] + [w''\theta''], \tag{3}$$

where $\overline{w'\theta'}$ represents the temporally-averaged vertical turbulent heat flux as measured by the eddy-covariance method at a single location, and $[w''\theta'']$ represents the spatially-averaged vertical turbulent heat flux as measured by the spatial method at any instant of time, respectively. Similarly, the first terms on the right-hand sides (r.h.s.) of Eqs. 2 and 3 represent the temporally- and spatially-averaged mean heat fluxes, respectively. Spatial averaging on Eq. 2, and temporal averaging on Eq. 3, yields

$$[\bar{F}] = [\bar{w}\bar{\theta}] + [\overline{w'\theta'}], \tag{4}$$

$$\overline{[F]} = \overline{[w][\theta]} + \overline{[w''\theta'']}, \tag{5}$$

where $[\bar{F}]$ is equal to $\overline{[F]}$, and is the so-called “true flux” or “representative flux”.

Over homogeneous surfaces, if the averaging period were sufficiently long, the turbulent-organized structures would be adequately sampled, and \bar{w} would approach zero. However,

in practice, the averaging period is often limited because of non-stationary effects in the atmosphere, such as the diurnal cycle, which causes \bar{w} to be non-zero (K04; S07; H08; S16) and, hence, results in a flux imbalance. In this sense, the flux imbalance over homogeneous surfaces is a result of failure to achieve statistical convergence.

In contrast, in the case of a Boussinesq fluid under periodic boundary conditions (as in our LES investigation, see Sect. 3.2), $[w]$ should be exactly equal to zero theoretically (S07). However, it should be noted that, in LES investigations, $[w]$ is not exactly equal to zero because of numerical errors, but is much smaller than the turbulent fluctuations. As such, to avoid the influence of numerical errors, past studies (K04; S07; H08; S16) treat the spatially-averaged vertical turbulent heat flux (i.e., $\overline{[w''\theta'']}$, which is the second item on the r.h.s. of Eq. 5), instead of the l.h.s. of Eq. 5, as the “true flux” or “representative flux”. The flux imbalance I at any grid point in the domain is then defined as

$$I(x, y, z) = \frac{\overline{w'\theta'} - \overline{[w''\theta'']}}{\overline{[w''\theta'']}}, \tag{6}$$

and the spatially-averaged flux imbalance $[I]$ is

$$[I] = \left[\frac{\overline{w'\theta'} - \overline{[w''\theta'']}}{\overline{[w''\theta'']}} \right] = - \left[\frac{\bar{w}\bar{\theta}}{\overline{[w''\theta'']}} \right]. \tag{7}$$

Here $[I]$ represents the “mean” difference between the temporal flux (i.e., the flux calculated from the eddy-covariance method) and the “true flux” or “representative flux” assuming that any grid point in the domain is equipped with a virtual eddy-covariance tower, and has been widely used as an index to quantify the flux imbalance related to the eddy-covariance method (K04; S07; H08; S16).

2.2 Flux Imbalance Over Heterogeneous Surfaces

A major difference between homogeneous and heterogeneous surfaces is that, while planar averaging (represented by the bracket) is commonly used over homogeneous surfaces to approximate the Reynolds averaging, we can only use spatial averaging in the homogenous direction to approximate the Reynolds averaging when the surface is heterogeneous. Here, we only consider heterogeneity in the x -direction, that is, the surface remains homogeneous in the y -direction, as is discussed in Sect. 3.2. Therefore, we use the spatial average over the y -direction (represented by the bracket with a subscript ‘ y ’, e.g., $[w]_y$) to approximate the Reynolds averaging. Moreover, the spatially-averaged vertical velocity component over the homogeneous direction (i.e., $[w]_y$) is not equal to zero largely because of mesoscale or secondary circulations, thereby invalidating the method in Sect. 2.1. As shown in Appendix 1, the value of the mean vertical velocity component over heterogeneous surfaces is much larger than the numerical error. As a result, the influence of numerical error on the spatially-averaged vertical velocity component $[w]_y$ is considered to be minimal over heterogeneous surfaces.

Based on the temporal decomposition (i.e., Eq. 3), we further decompose the local temporally-averaged field (e.g., \bar{w} and $\bar{\theta}$) into the spatial average of the time average (e.g., $[\bar{w}]_y$ and $[\bar{\theta}]_y$, where the subscript ‘ y ’ indicates the y -average) and the deviation from this spatial average (e.g., \bar{w}'' and $\bar{\theta}''$), yielding

$$\bar{F} = [\bar{w}]_y [\bar{\theta}]_y + \bar{w}'' \bar{\theta}'' + \bar{w}'' [\bar{\theta}]_y + \bar{\theta}'' [\bar{w}]_y + \overline{w'\theta'}. \tag{8}$$

The flux \bar{F} can then be either averaged over the homogeneous direction, or over the whole domain, as

$$[\bar{F}]_y = \left[[\bar{w}]_y [\bar{\theta}]_y \right]_y + \left[\bar{w}'' \bar{\theta}'' \right]_y + \left[\overline{w'\theta'} \right]_y, \tag{9}$$

$$[\bar{F}] = \left[[\bar{w}]_y [\bar{\theta}]_y \right] + \left[\bar{w}'' \bar{\theta}'' \right] + \left[\overline{w'\theta'} \right]. \tag{10}$$

While planar averaging does not approximate the Reynolds averaging, the flux averaged over the whole domain $[\bar{F}]$ here simply indicates a ‘representative’ flux over the heterogeneous surface, which is of most interest to us. Equation 10 is similar to Eq. 6 of Mahrt (2010) and Eq. 8 of I06. The first term on the r.h.s. of Eq. 10 is the vertical heat flux induced by the thermally-induced mesoscale circulations, which is equal to zero over homogeneous surfaces. The second term is the vertical heat flux induced by turbulent-organized structures, and the last term is the vertical turbulent heat flux as measured by the eddy-covariance method. It is noted that the vertical heat flux induced by turbulent-organized structures can be viewed as dispersive fluxes arising from the spatial correlations in the time-averaged field. That is, the spatial correlations induced by interactions between land-surface heterogeneity and turbulent structures contribute to the spatially-averaged flux. We note that this is different from canopy-flow studies, where dispersive fluxes arise from spatial averaging connected with canopy–fluid interactions (Raupach and Shaw 1982; Finnigan 2000). Here, the surface heterogeneity induces persistent spatial patterns (i.e., secondary circulations) that cannot be spatially averaged out.

The heat-flux fractions related to the thermally-induced mesoscale circulations Fr_{TMC} , turbulent-organized structures Fr_{TOS} , and small-scale turbulence Fr_{TU} (eddy-covariance method) can be expressed as

$$Fr_{TMC} = \frac{\left[[\bar{w}]_y [\bar{\theta}]_y \right]}{[\bar{F}]}, \tag{11}$$

$$Fr_{TOS} = \frac{\left[\bar{w}'' \bar{\theta}'' \right]}{[\bar{F}]}, \text{ and} \tag{12}$$

$$Fr_{TU} = \frac{\left[\overline{w'\theta'} \right]}{[\bar{F}]}, \tag{13}$$

respectively. If we follow the definition of the flux imbalance over homogeneous surfaces, the ‘representative’ flux imbalance $[I]$ over the heterogeneous domain is simply the sum of the mesoscale circulations and turbulent-organized-structure fractions as

$$[I] = \left[\frac{\left[\overline{w'\theta'} \right] - [\bar{F}]}{[\bar{F}]} \right] = -Fr_{TOS} - Fr_{TMC}. \tag{14}$$

Again, we perform the planar averaging here only to compare with the “mean” imbalance over a homogeneous domain of the same size. Note that, in all equations above, the parametrized subgrid fluxes should be added to the turbulent fluxes.

2.3 Relation Between the Flux Imbalance and Velocity Scales

Previous studies have shown the flux-imbalance magnitude to decrease with increasing wind speed (K04; S07) or friction velocity u_* (Stoy et al. 2013; S16). Further, H08 parametrized the

flux imbalance as a function of non-dimensionalized parameters related to turbulent velocity scales and source locations as

$$[I] = [\exp(a + bu_*/w_*) + c] \left[1.1 + d \left(\frac{z}{z_i} + f \right)^2 \right]^{0.5}, \quad (15)$$

where $a=4.2$, $b=-16$, $c=2.1$, $d=-8.0$ and $f=-0.38$ are fitted parameters. Here, u_* is the friction velocity, and w_* is the convective velocity defined as

$$w_* = \left(\frac{g}{\rho} z_i \frac{H}{c_p \theta_0} \right)^{\frac{1}{3}}, \quad (16)$$

where g is the acceleration due to gravity, ρ is the air density, θ_0 is a reference potential temperature, c_p is the specific heat of air, and z_i is the boundary-layer height. Based on Eq. 15, the flux-imbalance magnitude at a specific height can be expressed as

$$[I] = m [\exp(a + bu_*/w_*) + c], \quad (17)$$

where m is a constant value. Considering that the eddy-covariance tower has instrumentation installed at specific heights, we only examine here the variations of flux imbalance with u_* , w_* and u_*/w_* at a specific height. In addition to u_* and w_* , we also examine the relation between the flux imbalance and turbulent kinetic energy (TKE) defined as

$$\bar{e} = 0.5 (\sigma_u^2 + \sigma_v^2 + \sigma_w^2), \quad (18)$$

where \bar{e} is the TKE, and σ_u^2 , σ_v^2 , and σ_w^2 are the variances of the horizontal (u , v) and vertical (w) velocity components, respectively.

3 Experimental Design

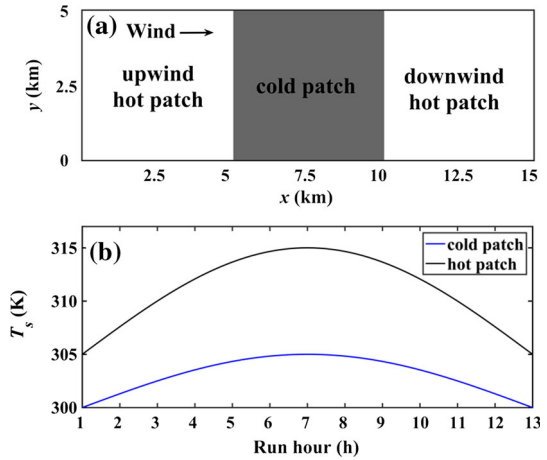
3.1 Model Description and Configuration

The simulations were performed with the Weather Research and Forecasting model (WRF) model version 3.8.1., which has LES capability, and has been widely used to investigate CBL characteristics under homogeneous and heterogeneous conditions (Patton et al. 2005; Moeng et al. 2007; Talbot et al. 2012; Zhu et al. 2016). Following Zhu et al. (2016), the original WRF-LES model is modified so that surface temperature, instead of the surface heat flux, may be prescribed as the boundary condition. The details of the modification can be found in Zhu et al. (2016).

We simulated a dry atmosphere over a flat, desert (hot) surface. For certain cases, surface heterogeneity was introduced by having an oasis (cold) patch in the middle of the domain (see Fig. 1) to mimic the field experiments conducted in the middle reaches of the Heihe River Basin (Li et al. 2013, 2016; Cheng et al. 2014). Except for the surface-layer scheme, other physical schemes in the WRF-LES model, such as microphysical and radiation parametrizations, were all turned off. In the surface-layer parametrization, Monin-Obukhov similarity theory was used to compute the sensible heat flux from the prescribed surface temperature and the simulated air temperature. The aerodynamic roughness length of the desert (hot) and oasis (cold) patches was set to 0.01 m and 0.1 m, respectively, and the thermal roughness length was parametrized using the surface-layer scheme in the WRF model (Zhu et al. 2016).

Periodic boundary conditions were used in our simulations. In addition, we used the default WRF model numerical discretization options (i.e., a fifth-order scheme for advection

Fig. 1 **a** The simulation domain and **b** the diurnal variations of surface temperature over hot and cold patches for case HE



in the horizontal direction, a third-order scheme for advection in the vertical direction, and a third-order Runge–Kutta scheme for the time integration). For the subgrid-scale turbulence parametrization, the 1.5-order TKE-based closure scheme was used. The simulation domain was $15 \text{ km} \times 5 \text{ km} \times 3 \text{ km}$ in the x , y and z directions and the number of grid points was $300 \times 100 \times 100$, giving a resolution in both the x and y directions of 50 m, and ranging from approximately 6–50 m in the z -direction (Talbot et al. 2012). The timestep was set to 0.5 s. The effects of the horizontal resolution and vertical grid stretching are discussed in Appendix 2. The model was initialized with an idealized neutral boundary-layer profile in which the potential temperature is 298 K below 850 m, and a strong inversion layer with a potential-temperature gradient of 60 K km^{-1} existing from 850 to 1050 m; the profile has a potential-temperature gradient of 3 K km^{-1} above 1050 m. All cases had the same initial atmospheric conditions.

3.2 Numerical Experiments

We design two cases to analyze the effects of spatial and diurnal variations of surface temperature on the flux imbalance. The key information of these cases is summarized in Table 1.

Table 1 Summary of the experiments

| Case | Simulation | Geostrophic wind speed (m s^{-1}) | Surface temperature (K) hot versus cold |
|------|------------|--|---|
| HO | HO_0 | 0 | $305 + 10 \sin t$ |
| | HO_1 | 1 | |
| | HO_10 | 10 | |
| HE | HE_0 | 0 | $305 + 10 \sin t$ versus $300 + 5 \sin t$ |
| | HE_1 | 1 | |
| | HE_10 | 10 | |

The first case is designed to analyze the effects of the diurnal variation of surface temperature over homogeneous surfaces (case HO) using a hot desert patch in the whole domain and a surface temperature based on a sinusoidal function with a mean value of 305 K, an amplitude of 10 K, and a period of 24 h (Fig. 1). The simulation is only performed in the daytime so as to avoid stable conditions at night requiring higher temporal and spatial resolutions (Beare et al. 2006; S07).

The second case is designed to analyze the effects of the diurnal variation of surface temperature over heterogeneous surfaces (case HE), for which the surface has different temperatures over the desert and the oasis. The oasis or cold patch is located between the two desert or hot patches, the size of each patch is identical (5 km \times 5 km) (Fig. 1), and both the oasis (cold) and desert (hot) patches are homogeneous in the y -direction. Note that the horizontal scale is about five times the ABL height to allow mesoscale circulations to develop (Patton et al. 2005). While the diurnal variation of surface temperature over the desert (hot patch) is the same as that in case HO, over the oasis (cold patch), the mean surface temperature and amplitude are reduced to 300 and 5 K, respectively (Fig. 1). These values are obtained by averaging observations collected on fair-weather days from 2012 to 2014 in the desert (hot patch) and oasis (cold patch) meteorological stations located in the middle reaches of the Heihe River Basin (Li et al. 2013, 2016; Xu et al. 2013).

To study the effects of the geostrophic wind speed, for each case we perform three simulations with a geostrophic wind speed of zero, 1 and 10 m s⁻¹ in the x -direction. The simulations with zero geostrophic wind speed represent free convective conditions, while those with non-zero geostrophic wind speed represent shear convective conditions. Each simulation is denoted “case_wind”, where, for example, “HO_1” refers to the HO case with 1 m s⁻¹ geostrophic wind speed. Note that, in the following, “simulation” refers to one simulation with a specific geostrophic wind speed, while “case” refers to all three simulations under the same surface setting (i.e., HO_0, HO_1, and HO_10 are all referred to as the HO case). Based on the wind direction, the hot patches are separated into “upwind hot patch” and “downwind hot patch”.

In all simulations, the diurnally-varying surface temperature is imposed after 2 h of integration time with the period < 2 h treated as model spin-up (Patton et al. 2005). The temporal statistics are computed for all grid points, i.e., all the grids in the domain are considered as virtual towers. The output frequency was 1 min, and the effects of different output frequencies are discussed in Appendix 3.

4 Results and Discussion

4.1 Homogeneous Case

4.1.1 The Diurnal Variation of Flux Imbalance in Case HO

Before examining the flux imbalance under the influence of the diurnal variation of surface temperature, Fig. 2a–d shows the surface (T_s) and air (T_a) temperatures, the surface heat flux H , the ABL height z_i , and convective velocity scale w_* for the case HO. As the surface warms, the air temperature increases with time, and becomes even higher than the surface temperature in the last 1 h (HO_0 and HO_1) or the last 2 h (HO_10) of simulation, resulting in slightly negative heat fluxes. The surface heat flux also shows a diurnal cycle, but reaches its peak value about 1 h earlier than the surface temperature. Due to the surface heating, the

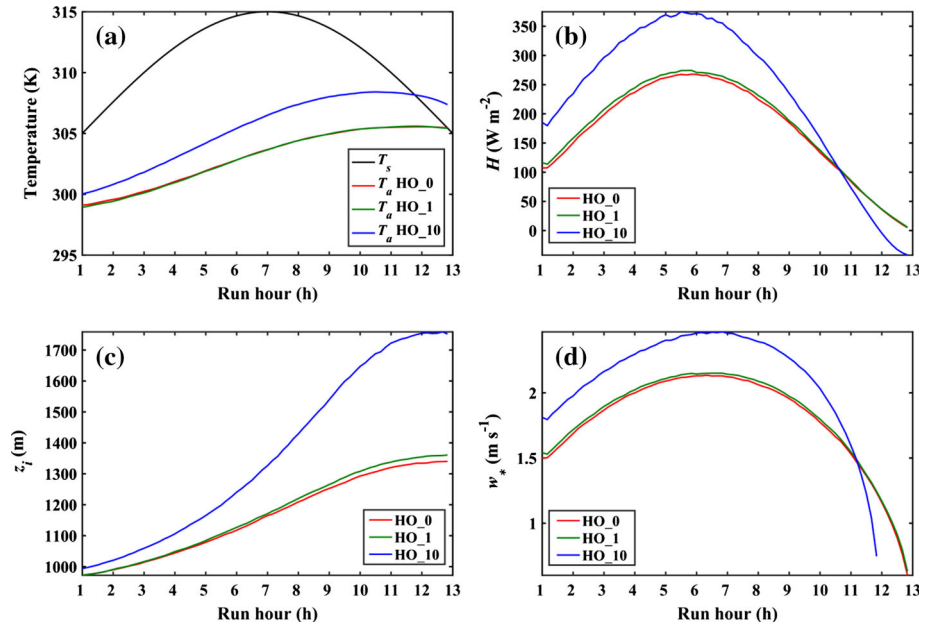


Fig. 2 a Surface temperature T_s , air temperature T_a , b surface heat flux H , c boundary-layer height z_i and d convective velocity scale w_* for case HO

value of z_i continues to increase with time, and reaches its largest value in the last hour, while the value of w_* increases first and then decreases, which mimics the temporal variation of the surface heat flux. The convective velocity w_* is not well-defined when the surface heat flux is negative and hence is not shown. Because of the stronger turbulence due to shear, the value of H in HO_10 is much larger than that in HO_0 and HO_1, which also leads to larger values of T_a , z_i and w_* .

As higher temporal and spatial resolutions are needed to resolve the large-scale turbulence when the atmosphere is stable, we only analyze results under unstable conditions (e.g., the first hour to the eleventh hour in the HO_0 and HO_1 simulations, and the first hour to the tenth hour in the HO_10 simulation).

Figure 3a shows the diurnal variations of the flux-imbalance magnitude at 103 m in case HO. The trends of the flux-imbalance magnitude at other heights are similar to that at 103 m and, hence, are not shown. The flux imbalance is -10% (-2%) at 28 m and -19% (-7%) at 103 m in the first hour in HO_0 (HO_1). As our simulated flux imbalance is very close to the E1 case (-20% at 100 m with zero wind speed) and E2 case (-9% at 100 m with $1 m s^{-1}$ wind speed) in K04 and the C1 case (-8% at 30 m with zero wind speed) in S07, with similar surface heat fluxes of about $0.10 K m s^{-1}$, this indicates that our results are robust. Consistent with field observations, the flux-imbalance magnitude decreases significantly with increasing geostrophic wind speed (Stoy et al. 2013) because with a larger the mean wind speed, more eddies are sampled using the eddy-covariance method for a given averaging period.

The flux imbalance has a clear diurnal cycle in free convective conditions (i.e., in the HO_0 simulation), and its magnitude decreases with increasing surface temperature and vice versa. However, with non-zero geostrophic wind speed (in the HO_1 and HO_10 simulations), the

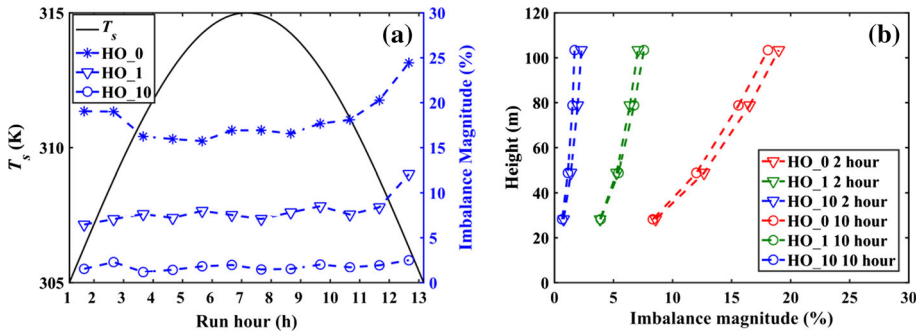


Fig. 3 **a** Diurnal variations of flux-imbalance magnitude for case HO, and **b** vertical profiles of flux-imbalance magnitude in the second and tenth hours for case HO

diurnal variation of the flux imbalance becomes very small, with the flux imbalance increasing slightly with time. Interestingly, the observed diurnal variation of the flux imbalance in shear convective conditions is different from S16, which used field observations to drive the LES model, and found the flux imbalance to decrease during the morning, before increasing during the afternoon. The diurnal variation of geostrophic wind speed (He et al. 2013) may be responsible for such differences, as is discussed further in Sect. 5.1.

In addition, the flux-imbalance magnitude increases with height up to about 100 m (Fig. 3b), which is in agreement with other studies (K04; S07), and further increases beyond 100 m, which is similar to the results in H08. This increasing trend is caused by the turbulent-organized structures becoming large and stronger as z increases. Given that our focus is on the flux imbalance near the surface, we do not investigate the flux imbalance at heights > 100 m herein. Figure 3b illustrates the increase in flux imbalance with height both in the morning and afternoon, and with similar slopes. While we also examined the flux imbalance with different averaging periods and different filter methods, the results are similar to those reported in previous studies (S16) and are thus not shown. In the following, an averaging period of 1 h is used if not stated otherwise.

4.1.2 Relations Between Flux Imbalance and Turbulent Velocity Scales

Based on our simulations (see Fig. 3) and previous studies (K04; S07; S16), the flux-imbalance magnitude decreases with increasing geostrophic wind speed (K04; S07) or u_* (Stoy et al. 2013; S16); H08 found the flux-imbalance magnitude decreases with increasing u_*/w_* over homogeneous surfaces. Motivated by these analyses, we examine the variations of flux imbalance with u_* , w_* and u_*/w_* when the diurnal variations are included (see Fig. 4).

The flux-imbalance magnitude decreases with increasing u_* and u_*/w_* , which is consistent with both previous studies (H08; Stoy et al. 2013; S16) and the expectation that more eddies are sampled for a larger geostrophic wind speed. Although the coefficients of the fitted functions are different from those in H08 (Fig. 4c), the same functional form used in H08 captures our results, which indicates that the relation between the flux imbalance and the ratio u_*/w_* is also valid with a diurnal variation of surface heat flux. The different coefficients are probably caused by the consideration of the diurnal variation and the fact that only two geostrophic wind speeds are considered herein.

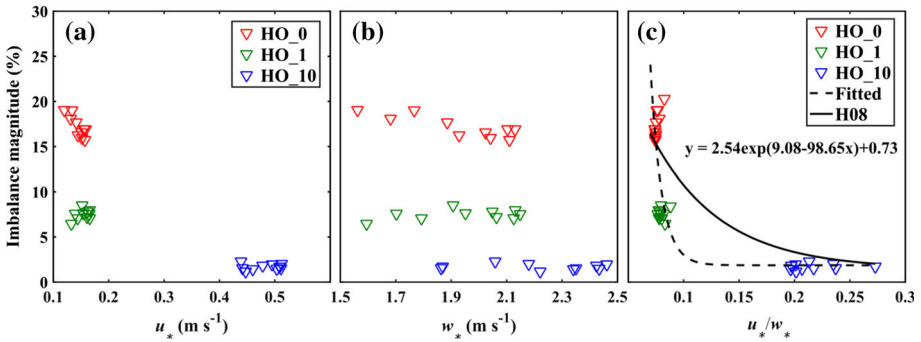


Fig. 4 The scatter plot of flux-imbalance magnitude at 103 m versus **a** u_* , **b** w_* , and **c** u_*/w_* for case HO. The dash line in panel c is the fitted line determined using the least-squares method and the black line represents the fitted result from H08

Furthermore, the flux-imbalance magnitude seems to vary little, or to slightly increase, with increasing w_* values, except under free convective conditions where the flux-imbalance magnitude decreases with increasing w_* . This result is similar to that in S07, where the flux-imbalance magnitude decreases with increasing surface heat flux in free convective conditions, and increases with increasing surface heat flux in shear convective conditions.

4.2 Heterogeneous Case

In this section, we analyze the combined effects of diurnal and spatial variations of surface temperature on the flux imbalance. Before we present the flux-imbalance results, the secondary circulations induced by thermal inhomogeneity are illustrated in Fig. 5, which shows the vertical cross-section of the y -direction- and time-averaged wind speed at the sixth hour in case HE. When the geostrophic wind speed is zero, there are clear secondary circulations between the hot and cold patches where the air sinks over the cold patch and flows from the cold patch to the adjacent hot patches before rising. The convergence occurs at the centre of the hot patch (i.e., at $x = 0$ or 15 km). With a 1 m s^{-1} geostrophic wind speed, the convergence occurs at the border between the upper hot patch and the cold patch. However, with a geostrophic wind speed of 10 m s^{-1} , the secondary circulation is diminished, which is consistent with previous studies (Crosman and Horel 2010; Zhang et al. 2014; Zhu et al. 2016).

4.2.1 The Diurnal Variation of Flux Imbalance in Case HE

Figure 6 shows the temporal variations of surface heat flux over different patches in case HE, with results in case HO also shown for comparison. As expected, the surface heat flux over the hot patch in case HE has a similar trend to that in case HO except with a larger magnitude because of the higher surface wind speed induced by surface heterogeneity. Although the surface heat flux over the hot patch is close to zero in the final hour, its value is not negative in the HE_10 simulation, which is different from that in the HO_10 simulation.

Over the cold patch, the surface heat flux is much lower than that over the hot patch and in case HO. Moreover, the surface heat flux over the cold patch decreases with increasing wind speed, which is opposite to the relation over the hot patch. As a result, the difference of surface heat flux between the hot and cold patches increases with increasing wind speed,

Fig. 5 Vertical cross-sections of y-direction-averaged wind speed and potential temperature at the sixth hour for case HE. The red and blue thick lines at the very bottom of **c** represent the hot and cold patches, respectively

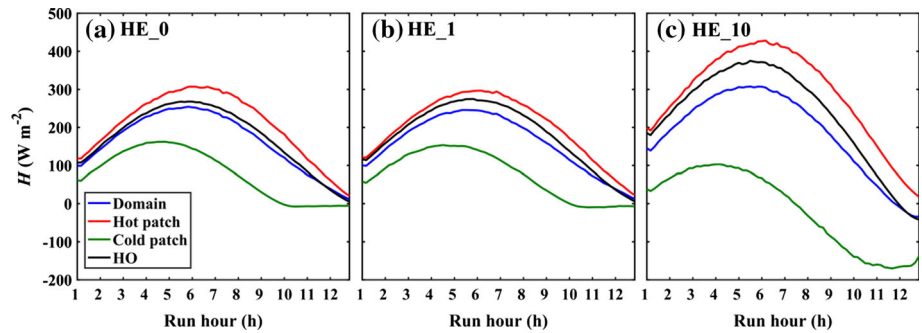
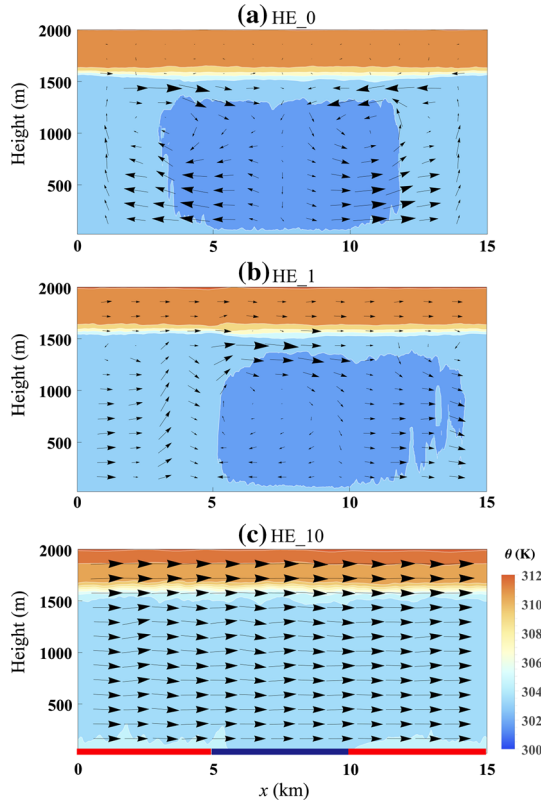


Fig. 6 The diurnal variations of surface heat flux for cases HE and HO

and reaches as much as $\approx 300 \text{ W m}^{-2}$ in the HE₁₀ simulation. The main reason is that an internal boundary layer is formed over the cold patch due to secondary circulations and, hence, the warmer air moves aloft over the cold patch, which then reduces the difference between surface temperature and air temperature and, thus, the heat flux over the cold patch. Therefore, the surface heat flux over the cold patch also reaches its peak value about 1 h earlier than that over the hot patch.

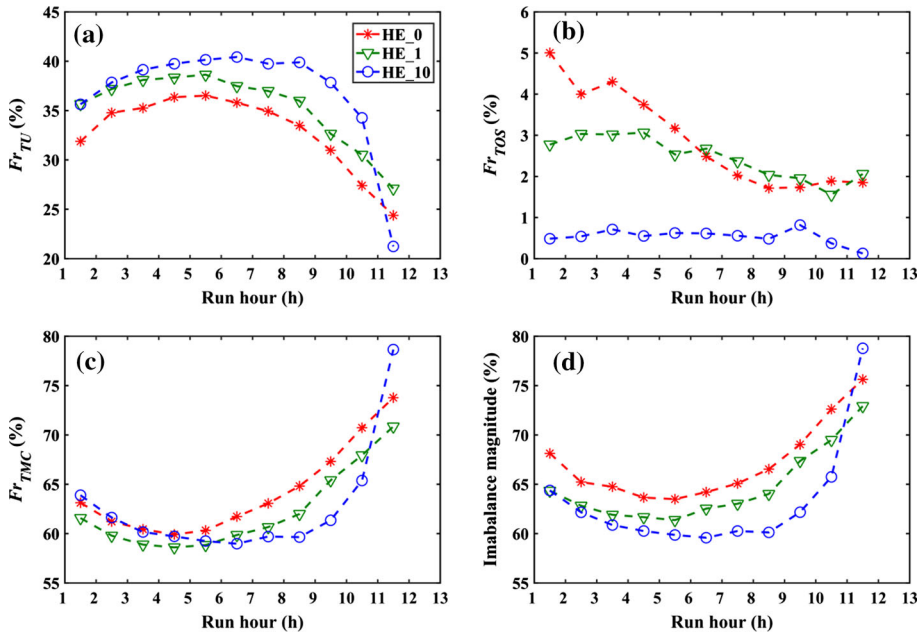


Fig. 7 The diurnal variations of **a** Fr_{TU} , **b** Fr_{TOS} and **c** Fr_{TMC} values and **d** the total imbalance magnitude (i.e., the sum of the fractions Fr_{TOS} and Fr_{TMC}) for case HE

The domain-averaged surface heat flux is smaller than that over homogeneous surfaces because of the smaller surface heat flux over the cold patch. As with case HO, in the following sections, we only show results in unstable conditions.

Figure 7 shows the temporal variations of the heat-flux fractions (a) Fr_{TU} , (b) Fr_{TOS} and (c) Fr_{TMC} , and (d) the total flux-imbalance magnitude (i.e., the sum of Fr_{TOS} and Fr_{TMC}) in case HE. Values of Fr_{TOS} are $<5\%$, and slightly decreasing with time, which differs from case HO not only in terms of the magnitude but also in terms of the trend. The Fr_{TMC} values are larger than 55% , decrease before the fifth hour, and then increase until the boundary layer becomes stable over the cold patch. The temporal variation of the total flux imbalance is very close to the temporal variation of Fr_{TMC} values because the magnitude of Fr_{TOS} is so small. This result confirms that it is probably thermally-induced mesoscale circulations, and not turbulent-organized structures, that mainly contribute to the flux imbalance in the field (Foken 2008; Foken et al. 2011; Stoy et al. 2013). The same trend was also observed in I06, but the flux imbalance here is larger than that in I06, probably because the scale of surface heat-flux variation was 8 km in I06, which is smaller than the scale of surface temperature variation here (about 10 km). Moreover, the secondary circulations in our simulations are stronger than those in I06.

With an increasing geostrophic wind speed, the flux-imbalance magnitude decreases, which is similar to that in case HO. However, it is interesting to note that, with increasing geostrophic wind speed, the diurnal variation of flux imbalance in case HE remains evident, which is different from the results in case HO where the diurnal variation of flux imbalance is greatly damped by the increased geostrophic wind speed. This indicates that secondary circulations induced by surface heterogeneity not only alter the magnitude of flux imbalance, but also its temporal variation.

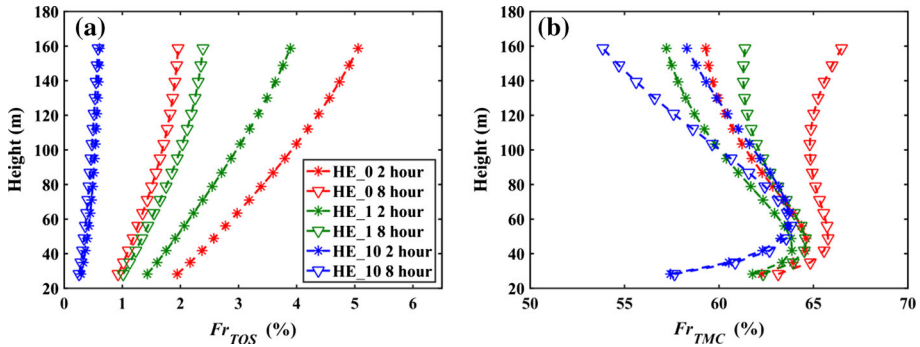


Fig. 8 The vertical profiles of **a** Fr_{TOS} and **b** Fr_{TMC} values in the second and eighth hours in the HE_0 simulation

The height dependence is different for the Fr_{TOS} and Fr_{TMC} values (Fig. 8), with Fr_{TOS} values in case HE increasing with height (Fig. 8a), similarly to case HO (Sect. 4.1, Fig. 3b) and other studies (K04; S07; S16). In contrast, the Fr_{TMC} values increase with height at lower heights, and then decrease with height at greater heights (Fig. 8b), which is mainly due to the increase in the mean vertical velocity component at lower heights. Because of the dominant role of mesoscale circulations, the dependence of the flux imbalance on height is similar to that of the Fr_{TMC} values.

4.2.2 Relations Between Flux Imbalance and Turbulent Velocity Scales

Similar to Sect. 4.1.2, here we examine the relationship between the flux imbalance and the parameters u_* , w_* , and u_*/w_* over heterogeneous surfaces (Fig. 9). While we acknowledge that secondary circulations are forced by the temperature difference between different patches, the parameters u_* , w_* and u_*/w_* are selected here to compare with the results over homogeneous surfaces. We also note that other studies also used the parameter u_*/w_* to scale the flux imbalance over heterogeneous surfaces (Eder et al. 2014).

The dependencies of the flux fractions Fr_{TMC} and Fr_{TOS} on u_* , w_* and u_*/w_* are significantly different. For example, Fr_{TOS} values decrease with increasing u_* and u_*/w_* , similarly to case HO. With increasing w_* , however, the Fr_{TOS} values decrease in some periods (first hour to fifth hour) but increase in other periods (sixth hour to eighth hour) in the HE_0 and HE_1 simulations, while exhibiting a hysteresis pattern. In contrast, the dependence of the Fr_{TMC} values on the variables u_* , w_* and u_*/w_* is complex. Although the Fr_{TMC} values decrease with increasing w_* , overall, there is a strong hysteresis between these two variables. Meanwhile, there is no obvious relation between Fr_{TMC} values and the parameters u_* and u_*/w_* .

The results above indicate that u_*/w_* is probably a good scaling parameter for the flux fraction Fr_{TOS} , but not for Fr_{TMC} . Given the dominant role of mesoscale circulations on the flux imbalance over heterogeneous surfaces, the flux-imbalance magnitude is not well captured by the parameter u_*/w_* , which may be the reason for the failure of this relationship in the field (Eder et al. 2014).

4.2.3 The x-Dependence of Flux Imbalance

Sections 4.2.1 and 4.2.2 examined the domain-averaged flux imbalance over heterogeneous surfaces since the focus there was the “representative” flux imbalance. However, it is interest-

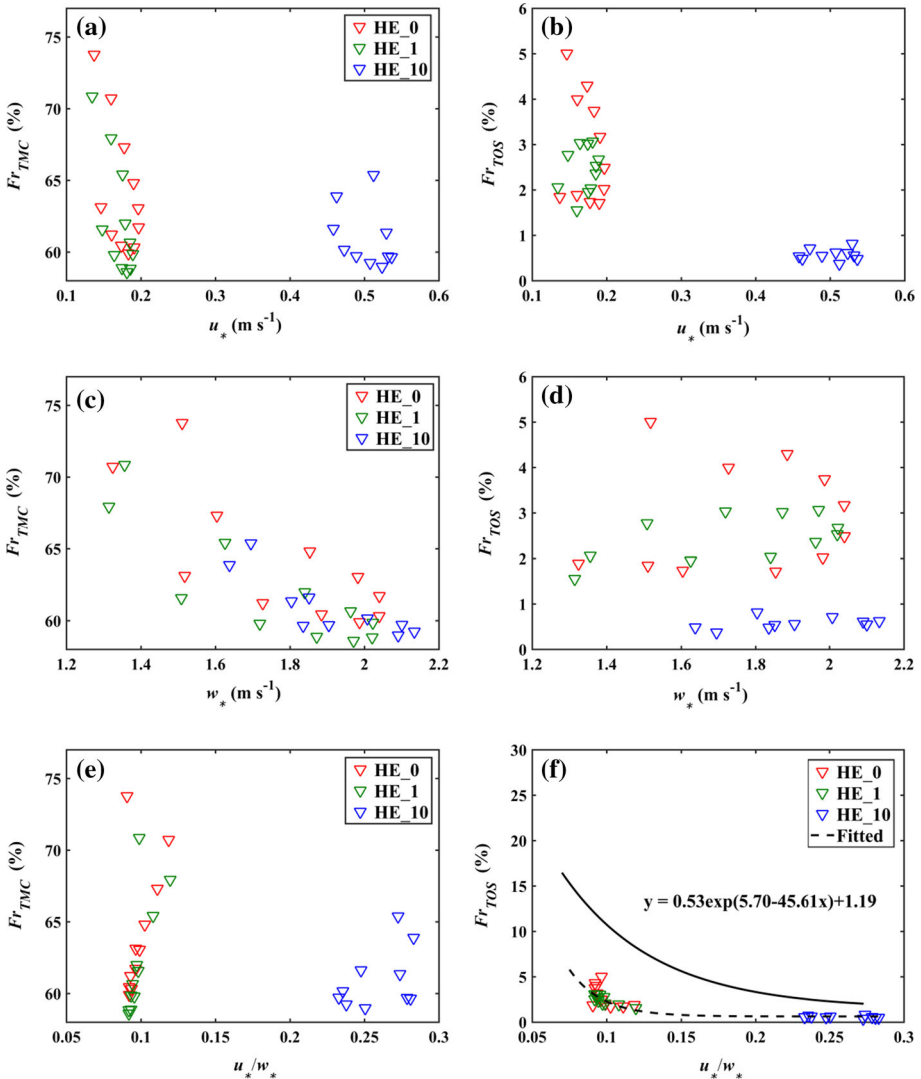


Fig. 9 The values of **a, c** Fr_{TMC} and **b, d** Fr_{TOS} at 103 m versus **a, b** w_* , **c, d** u_* and **e, f** u_*/w_* . The dashed line in **f** is determined using the least-squares method, and the black line represents the fitted result from H08

ing to examine the x -dependence of the flux imbalance over heterogeneous terrain. Figure 10 shows the three \bar{w} terms on the r.h.s. of Eq. 9 (i.e., $[\bar{w}]_y [\bar{\theta}]_y$, $[\bar{w}'' \bar{\theta}'']_y$, and $[\bar{w}' \theta']_y$) along the x -direction (wind direction) during the fifth hour at 103 m in case HE, which are denoted as TMC_y , TOS_y , and TU_y , respectively, below.

Under free convective conditions, TU_y changes most dramatically (with a 50% drop) at the edges of the cold patch (i.e., at $x = 5$ and 10 km). With a larger geostrophic wind speed, the location of this abrupt decrease moves downwind, especially in the HE_10 simulation (Fig. 10a). There is no clear trend in the x -dependence of TOS_y due to its small magnitude and large variability, especially in the HE_0 and HE_1 simulations (Fig. 10b). Similarly, the

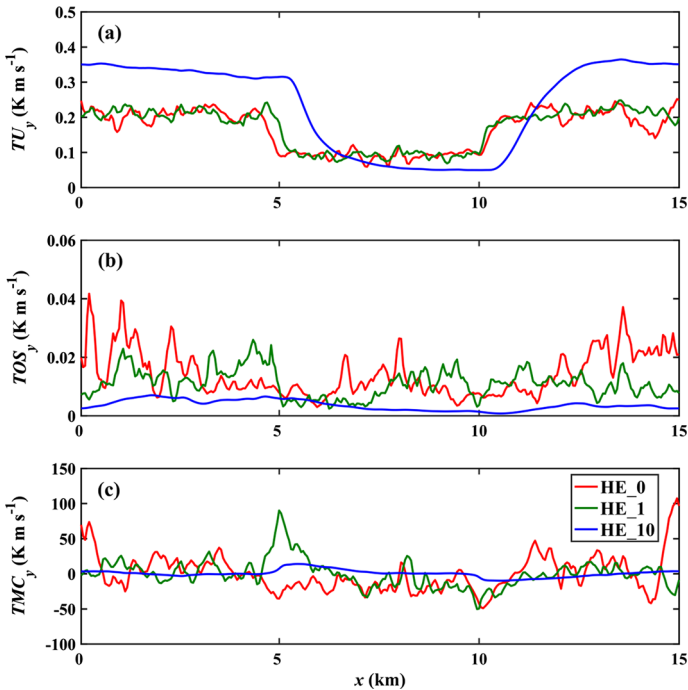


Fig. 10 Values of the terms **a** TU_y , **b** TOS_y and **c** TMC_y along the x -direction (i.e., wind direction) at 103 m during the fifth hour for case HE

behaviour of TMC_y has no clear trend along the x -direction because of its large variability in the HE_0 and HE_1 simulations (Fig. 10c). Note that, at higher geostrophic wind speeds, both components of flux imbalance (i.e., TMC_y and TOS_y) become fairly uniform along the x -direction.

5 Discussion

5.1 Comparing Observed and Simulated Diurnal Variations of Flux Imbalance

Using data from the FLUXNET sites across 173 ecosystems, Stoy et al. (2013) found that the increase of the energy-balance closure ratio (the ratio of the sum of turbulent heat fluxes to the available energy) is less in the morning than the corresponding decrease in the afternoon, implying the flux-imbalance magnitude decreases slowly in the morning and increases more rapidly in the afternoon. However, the flux-imbalance magnitude was found to decrease throughout the daytime period by Wilson et al. (2002), who also analyzed data from 22 FLUXNET sites, and by Xu et al. (2017) at the HiWATER site.

Overall, our simulations show that the diurnal variations of flux imbalance in case HE and in the HO_0 simulation are similar to those in Stoy et al. (2013) and S16. More importantly, our results help understand why there are significant differences in the observed (Wilson et al. 2002; Stoy et al. 2013; Xu et al. 2017) and simulated (S16 and ours) diurnal variations of flux imbalance. One possible reason is the diurnal variation of the geostrophic wind speed.

For example, if the geostrophic wind speed were to increase (decrease) during the morning (afternoon), which is the case at the Cabauw site (He et al. 2013), the flux-imbalance magnitude would decrease (increase) during the morning (afternoon), which probably explains the behaviour of the flux-imbalance magnitude reported by S16. Another possible reason is that the unique atmospheric or land-surface conditions around these sites. Our simulations over both homogeneous and heterogeneous surfaces still cannot explain the diurnal variations of flux imbalance observed in Wilson et al. (2002) and Xu et al. (2017), suggesting that including surface heterogeneity (at least in the simplified fashion in our simulations) may be insufficient, making it necessary to also include site-specific information in LES investigations. For example, there are different landscape patches, such as shelterbelts, croplands, and roads around the eddy-covariance site in Xu et al. (2017), and human activities, such as irrigation, which may also affect the diurnal variation of the flux imbalance.

We have not considered the latent heat flux, whose diurnal behaviour may be different from the sensible heat flux, although the study of S16 showed that the diurnal variations of imbalance for sensible and latent heat are very similar (S16). Moreover, many processes in the field preferentially occur in the afternoon, such as clouds and precipitation, which not only affect the atmospheric conditions (e.g., the wind speed), but also the surface temperature and surface heat flux, which further affect the flux imbalance.

5.2 Relationships Between the Flux Imbalance and Flow Variables

While Sects. 4.1.2 and 4.2.2 examine the relations between the flux imbalance and turbulent velocity scales, the effect of the flow conditions on the diurnal behaviour of the flux imbalance is not explored. For example, the TKE decreases with time in the afternoon (Darbieu et al. 2015), which may affect the flux imbalance during the afternoon. Meanwhile, as found by De Roo and Mauder (2017), there is a correlation between the flux imbalance and the difference between the potential temperature and surface temperature (hereafter ΔT). Therefore, here we examine the relationships between the flux imbalance and TKE and ΔT values.

Figure 11 shows the variation in the flux-imbalance magnitude at a height of 103 m with the TKE in the HO_0 and HE_0 simulations. There is a clear diurnal cycle of TKE in both simulations, which, together with the afternoon decay of TKE, has also been observed and simulated by others (Sorbjan 1997; Goulart et al. 2003; Pino et al. 2006; Nadeau et al. 2011; Rizza et al. 2013; Darbieu et al. 2015). Following Darbieu et al. (2015), the afternoon decay of TKE starts at the maximum H value and ends when H reaches zero, corresponding to the fifth and twelfth hours, respectively (Fig. 11). As with previous studies, during the afternoon TKE decay, three phases exist (Fig. 11): (1) the first phase during which the value of H is maximum before decreasing while the TKE continues to increase slightly (the sixth hour); (2) the second phase during which the TKE decays at a low rate (the seventh hour to the tenth hour); and (3) the third phase characterized by a larger TKE decay rate (the eleventh to the twelfth hour) (Fig. 11).

The change of flux imbalance is clearly correlated with the change of TKE. In the first stage, the flux-imbalance magnitude is continually decreasing with increasing TKE, which is mainly caused by the fact that, although the value of H begins to decrease, the sensible heat flux is still large enough to heat the whole ABL (Darbieu et al. 2015), which induces the slight increase of TKE and, hence, the decrease in the flux-imbalance magnitude. During the second stage, the flux-imbalance magnitude begins to increase with the decay of H values and TKE. Compared with the first stage, the flux-imbalance magnitude increases sharply in this stage. The main reason is that, although the sizes of large eddies remain approximately constant during this stage (Darbieu et al. 2015), these large eddies are less energetic due to

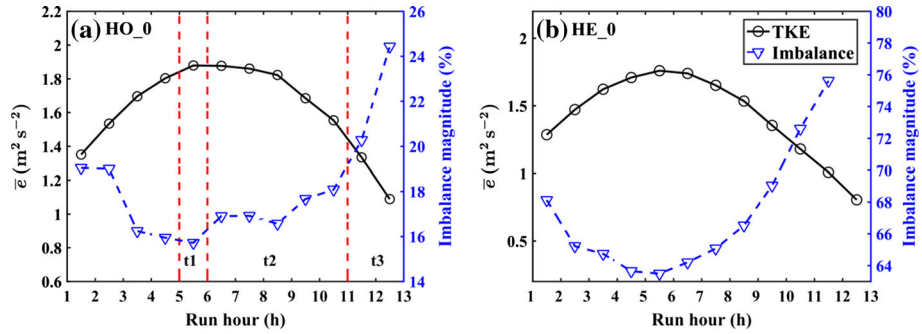


Fig. 11 The diurnal variations of TKE (left axis) and the flux-imbalance magnitude (right axis) at height 103 m in the **a** HO_0 and **b** HE_0 simulations. The periods labelled t1, t2 and t3 in panel **a** correspond to the three stages in the afternoon decay

the decay in the value of H and, hence, less eddies can be sampled, which leads to the larger flux imbalance. Following this stage, TKE rapidly decreases due to the very small H values, and, hence, turbulence is further weakened. Both factors cause the flux-imbalance magnitude to further increase in this stage.

In summary, the rapid decrease of TKE during the afternoon is responsible for the corresponding rapid increase of flux-imbalance magnitude. Moreover, there is a near-linear relation between TKE and the flux imbalance (Fig. 12a, b), with the larger the TKE, the smaller the flux-imbalance magnitude. With a non-zero geostrophic wind speed, the above conclusion is also valid over heterogeneous surfaces (Fig. 12a), whereas over homogeneous surfaces, the flux-imbalance magnitude becomes smaller and less affected by TKE (Fig. 12b).

Motivated by the results of De Roo and Mauder (2017), we also examine the correlation between the flux imbalance and the difference between the potential temperature and surface temperature ΔT (Fig. 12c, d). In contrast to De Roo and Mauder (2017), our simulations cover both free convective and shear convective conditions, and include both homogeneous and heterogeneous surfaces. Similar to their findings, there is also a clear relation between the flux imbalance and ΔT in our simulations over heterogeneous surfaces, despite large scatter. The larger the value of ΔT , the smaller the flux-imbalance magnitude (Fig. 12c), which suggests that the findings of De Roo and Mauder (2017) also apply to shear convective conditions. In contrast, there is no relationship between the flux imbalance and ΔT over homogeneous surfaces.

5.3 The Effect of Averaging Period and Filter Method

The dependence of the flux imbalance on different averaging periods and different filter methods over homogeneous surfaces is discussed in S16, where the flux imbalance is shown to be smaller with a longer averaging period, but larger using the linear detrending method than the block-average method. However, how the flux imbalance changes with different averaging periods and different filter methods over heterogeneous surfaces has not yet been investigated.

Figure 13 shows the temporal variation of the Fr_{TOS} and Fr_{TMC} values at 103 m using different averaging periods (15, 30, and 60 min) and different filter methods (block average and linear detrending) in the HE_0 simulation. The results in the other two simulations (HE_1 and HE_10) have a similar trend and are not shown. Different components of the flux

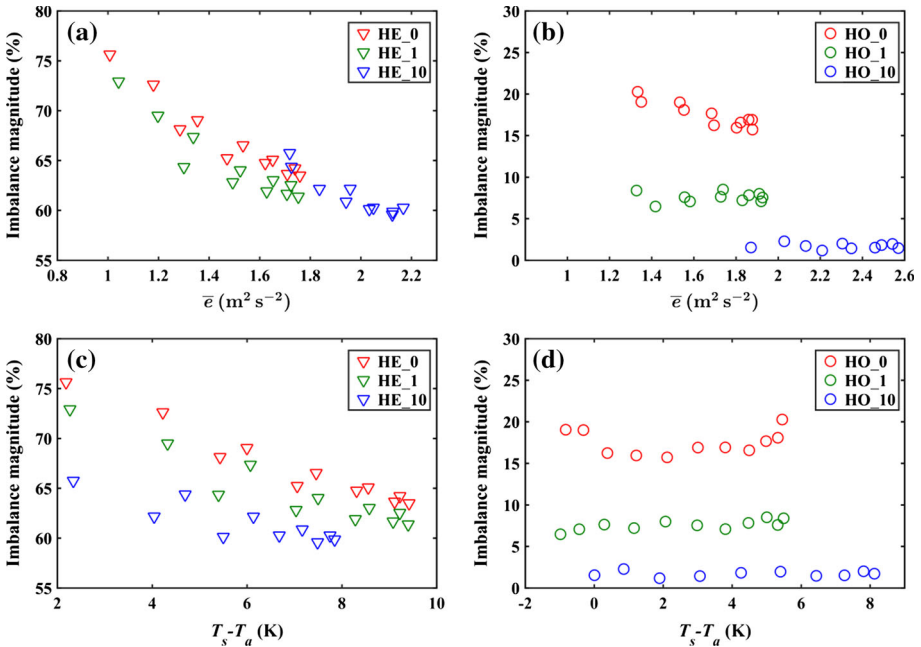


Fig. 12 The flux-imbalance magnitude at height 103 m versus **a, b** TKE and **c, d** the difference between surface temperature and air temperature in the **a, c** case HE and **b, d** case HO

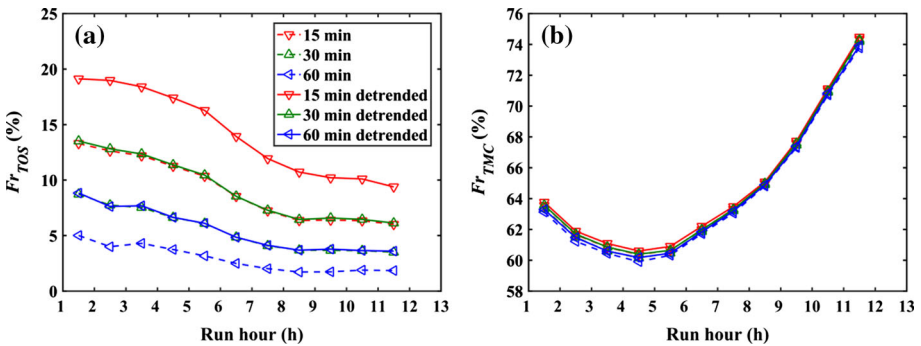


Fig. 13 The temporal variation of **a** Fr_{TOS} and **b** Fr_{TMC} values at height 103 m using different averaging periods (15, 30, and 60 min) and different filter methods (block average and linear detrending) for case HE

imbalance are affected differently by changing the averaging periods and filter methods. The Fr_{TOS} values decrease with longer averaging periods because a greater number of eddies is sampled by the eddy-covariance method and, hence, more contributions from larger eddies to the vertical turbulent heat fluxes are detected, rather than to the vertical heat fluxes induced by turbulent-organized structures.

Additionally, compared with the block-average method, the Fr_{TOS} values calculated using the linear detrending method are greater, since the linear detrending method is essentially a narrower high-pass filter than the block-average method, i.e., the linear detrending method removes a larger part of the turbulent eddies (Rannik and Vesala 1999; S16). Meanwhile,

it should be noted that the Fr_{TOS} values over 1 h using the linear detrending method are strikingly close to the Fr_{TOS} values using the block average over 30 min, i.e., the linear detrending method effectively halves the averaging period for the same flux imbalance, since removing the mean values of two consecutive periods is similar to removing the linear trend of the total period (S16).

Compared with the Fr_{TOS} values, Fr_{TMC} values are barely affected by the averaging periods and filter methods since the scale of mesoscale circulations is much larger than the filter scale of both methods. For example, the spatial scale of mesoscale circulations l is ≈ 5 km and the time scale based on the convective velocity scale w_* is ≈ 2500 s. Thus, within the averaging period (i.e., 1 h), the measurements include no more than two samples of mesoscale circulations. Therefore, the filter methods and averaging periods have almost no influence on the magnitude of Fr_{TMC} values.

5.4 Implications for Eddy-Covariance Observations at a Point

There are a few important implications for actual eddy-covariance observations. First, due to a non-zero \bar{w} , a flux imbalance exists over both homogeneous and heterogeneous surfaces. Over homogeneous surfaces, the non-zero \bar{w} is mainly caused by turbulent-organized structures while, over heterogeneous surfaces, the non-zero \bar{w} is mainly induced by secondary circulations. However, computing \bar{w} and $\bar{\theta}$ values at one point in the field for use as a proxy of the imbalance would be impractical for two reasons. One is that the mean vertical velocity component needs to be measured precisely (within 0.001 m s^{-1}) at the height of eddy-covariance observations (Lee 1998), which is challenging because the mean vertical velocity component measured by three-dimensional sonic anemometers is contaminated by even a small zero offset in the electronics and the sensor tilt relative to the terrain surface (Lee 1998). The other problem is that $\bar{w}\bar{\theta}$ values at a point are poorly correlated with the ‘representative’ flux imbalance $[I]$ as discussed by K04, especially because the local term $\bar{w}\bar{\theta}$ (i.e., measured at a single point) is usually much larger than the spatially-averaged term $[\bar{w}\bar{\theta}]$. Therefore, considering $\bar{w}\bar{\theta}$ values at a point is meaningless in estimating the representative flux $[\bar{F}]$ or the representative flux imbalance even if the three-dimensional sonic anemometers are well aligned and can measure \bar{w} precisely. In practice, the magnitude of \bar{w} is forced to zero through coordinate rotation or planar fitting (Aubinet et al. 2012), which does not completely erase the \bar{w} signal, explaining the existence of the flux imbalance after coordinate rotation or planar fitting.

Second, as shown in Fig. 3b, the flux imbalance increases almost linearly with height; close to the surface, the flux imbalance is approximately zero. In addition, as the Fr_{TMC} values and the flux-imbalance magnitude over heterogeneous surfaces increase with height in the lowest 100 m, eddy-covariance sensors should be installed at very low elevations. However, in practice, the eddy-covariance method requires several additional considerations. For example, the sensors should be installed above the roughness layer or in the “constant-flux layer”. Additionally, the flux underestimation induced by the separation between the vertical velocity sensor and a scalar sensor increases with decreasing eddy-covariance measurement height (Kristensen et al. 1997). Therefore, the lower the measurement height, the closer the sensors must be, which may cause further issues, such as flow distortions induced by scalar sensors. In short, the sensor height must be much larger than the separation distance between the velocity sensor and the scalar sensor, and in the constant-flux layer. Once these conditions are satisfied, a lower height is recommended.

Third, as discussed in Sect. 5.3, the magnitude of Fr_{TMC} values is barely affected by the averaging periods and filter methods, which indicates that, even with a longer averaging

period (e.g., 1 h), in practice it is hard to reduce Fr_{TMC} values. Lastly, the flux imbalance is found to be linearly related to the TKE and ΔT ; the larger the TKE and ΔT , the smaller the flux-imbalance magnitude. This indicates that the TKE and ΔT may be promising indicators for developing corrections for the energy-balance closure.

6 Conclusions

We have analyzed the separate and joint effects of temporal variability and spatial heterogeneity of surface temperature on the flux imbalance in a dry convective boundary layer. Over homogeneous surfaces, the flux imbalance is due to turbulent-organized structures, while over heterogeneous surfaces, the flux imbalance is mainly due to thermally-induced mesoscale circulations with minimal contributions from turbulent-organized structures. The main findings are:

- (1) The temporal variation of surface temperature leads to a diurnal variation of flux imbalance over homogeneous surfaces. For example, in free convective conditions, the magnitude of the flux imbalance decreases slowly during the morning period with increasing surface temperature, and increases rapidly during the late afternoon period with decreasing surface temperature. However, in shear convective conditions, both the flux-imbalance magnitude and its temporal variation are different. The magnitude of the flux imbalance is much smaller and slightly increases with time. Due to the small magnitude, this increasing trend is not significant.
- (2) Over heterogeneous surfaces, the temporal variation of the surface heat flux also leads to the temporal variation of the flux imbalance, which is similar to that over homogeneous surfaces in free convective conditions except with a larger imbalance, confirming that surface heterogeneity strongly increases the flux imbalance. Moreover, although the flux-imbalance magnitude decreases with an increasing geostrophic wind speed, the diurnal variations of flux imbalance are similar under different geostrophic wind speeds. Additionally, the turbulent-organized structures and thermally-induced mesoscale circulations contribute differently to the flux imbalance over heterogeneous surfaces. The Fr_{TOS} values continue to decrease with time while the Fr_{TMC} values have a clear diurnal cycle. Moreover, the afternoon decay of TKE is responsible for the increasing flux-imbalance magnitude of case HE during the afternoon.
- (3) Over both homogeneous and heterogeneous surfaces, the turbulent-organized structures can be scaled by the parameter u_*/w_* . However, over heterogeneous surfaces, there is no obvious relation between the flux imbalance and the parameters u_* or u_*/w_* . Interestingly, the flux imbalance is linearly related to TKE and ΔT over heterogeneous surfaces; the larger the TKE and ΔT values, the smaller the flux-imbalance magnitude. Compared with a previous study (De Roo and Mauder 2017), the above findings not only show that the flux-imbalance magnitude decreases with the increasing ΔT , but also confirm that this correlation is valid in both free and shear convective conditions. However, the above linear relation is invalid over homogeneous surfaces due to the small magnitude of flux imbalance in shear convective conditions.

Our study has a few limitations that are important to point out. Firstly, only a dry boundary layer is considered, and so the role of water vapour needs to be further determined. Second, it remains to be examined which turbulence characteristics control the scaling of the flux imbalance, making it necessary to examine the flux imbalance over a surface characterized by different heterogeneity scales and temperature differences between landscape patches. Third,

it should be noted that, although the diurnal variation of the flux imbalance over heterogeneous surfaces is consistent with the observed general trend across various ecosystems, the diurnal variation of the flux imbalance might be site-specific. Lastly, as the control-volume approach has also been used to calculate the flux imbalance, it may be necessary to examine the differences between our method and the control-volume approach (Finnigan et al. 2003), which is left for future investigations.

Acknowledgements This work was jointly supported by the National Natural Science Foundation of China (Grant: 91425303 and 41630856) and the Strategic Priority Research Program of the Chinese Academy of Sciences, Grant: XDA19070100. H.L. acknowledges support by National Science Foundation AGS under Grants: 1419614. The major part of this work was conducted when the first author visited Boston University in 2017. We thank Professor Guido Salvucci and Dr. Angela Rigden at Boston University for their constructive comments and suggestions.

Appendix 1: The Effect of Numerical Error

As stated in Sect. 2.1, we treat $[w]$ as identically zero in case HO. However, when the surface is heterogeneous, we must use the $[\bar{F}]$ as the “true flux” or “representative flux” (Sect. 2.2). Therefore, one question remains to be answered: how does the numerical error in $[w]$ affect the imbalance in case HE? Figure 14 shows the mean and standard deviation of the vertical velocity component in the HO and HE cases at 28 m during the first hour. The inset shows the mean and standard deviation of the vertical velocity component in case HO because the value is too low. As the numerical error is clearly four orders of magnitude smaller than the simulated vertical velocity component over heterogeneous surfaces, the effects of numerical errors in case HE can be safely neglected.

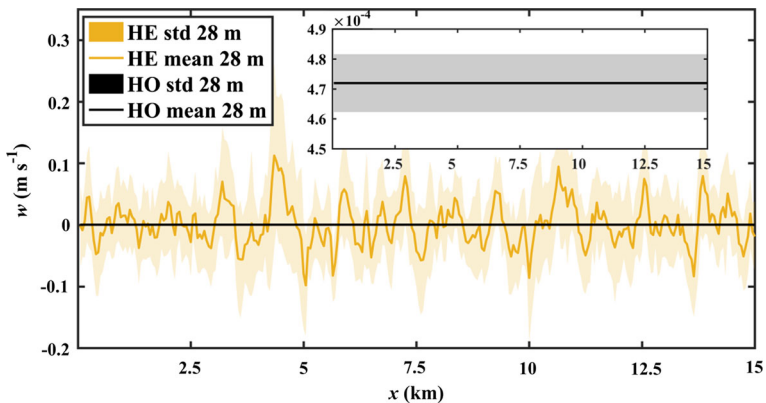


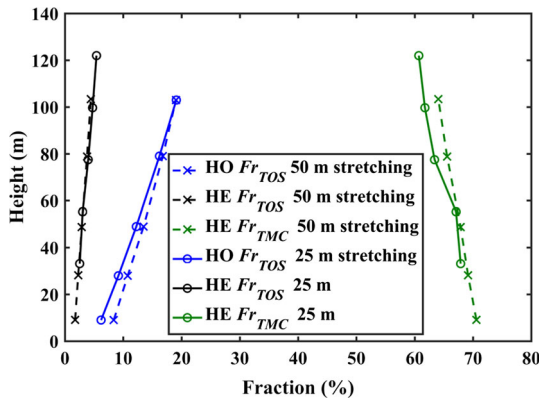
Fig. 14 The mean and standard deviation (std) of the vertical velocity component in the HO and HE cases at 28 m during the first hour. The inset is the mean and standard variation of the vertical velocity component in case HO

Appendix 2: Sensitivity to Resolution and Vertical Stretching

To examine the sensitivity to the resolution, additional simulations were conducted at a finer horizontal grid resolution of $25\text{ m} \times 25\text{ m}$ in the first hour of the HO and HE cases. Also, to examine the sensitivity to the vertical stretching, the additional simulations employed a constant vertical grid resolution of 25 m for the HE case, but a vertically-stretched grid for the HO case.

The Fr_{TOS} and Fr_{TMC} values in the HO and HE cases at different heights are shown in Fig. 15, where little difference between the simulated results from the two grids of different horizontal resolutions is evident, with a mean absolute difference of 1.2%. Similarly, the effects of vertical grid stretching on Fr_{TOS} and Fr_{TMC} values are also small, with a mean absolute difference of 1.27%. Therefore, a grid with a horizontal resolution of $50\text{ m} \times 50\text{ m}$, and stretched in the vertical direction is used.

Fig. 15 The Fr_{TOS} and Fr_{TMC} values at different heights with different horizontal and vertical resolutions



Appendix 3: Sensitivity to Output Frequency

To examine the sensitivity to the output frequency, w and θ values are produced every 1, 60, 300 and 600 s in the first hour of the HO case. The probability density function and statistics of the imbalance at different heights are shown in Fig. 16 and Table 2, where little difference in the results of 1-s and 1-min output frequencies is illustrated, with a mean absolute difference ratio of 2%. The difference is larger when the output frequency becomes larger than 60 s, with a mean absolute difference ratio of 22% at 300 s and 47% at 600 s. Therefore, outputs of w and θ values are produced every minute to save storage space without affecting the final results.

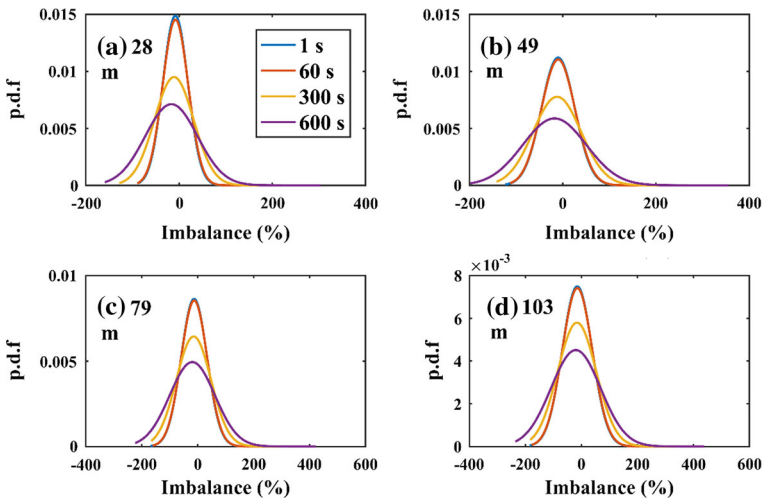


Fig. 16 The probability density function (p.d.f.) of flux imbalance calculated with different output frequencies in case HO

Table 2 The statistics of the flux imbalance in case HO with different output frequencies; std denotes the standard deviation

| Time interval (s) | 28 m | | 49 m | | 79 m | | 103 m | |
|-------------------|----------|---------|----------|---------|----------|---------|----------|---------|
| | Mean (%) | Std (%) | Mean (%) | Std (%) | Mean (%) | Std (%) | Mean (%) | Std (%) |
| 1 | -9 | 27 | -11 | 36 | -17 | 46 | -19 | 53 |
| 60 | -9 | 31 | -11 | 35 | -18 | 46 | -20 | 57 |
| 300 | -12 | 42 | -15 | 51 | -20 | 62 | -21 | 69 |
| 600 | -16 | 56 | -17 | 68 | -23 | 81 | -24 | 88 |

The averaging period is 1 h

References

- Aubinet M, Vesala T, Papale D (eds) (2012) Eddy covariance: a practical guide to measurement and data analysis. Springer, Dordrecht
- Beare RJ, Cortes MAJ, Cuxart J, Esau I, Golaz C, Holtstlag AAM, Khairoutdinov M, Kosovic B, Lewellen D, Lund T, Lundquist J, McCabe A, Macvean MK, Moene A, Noh Y, Poulos G, Raasch S, Sullivan PP (2006) An intercomparison of large-eddy simulations of the stable boundary-layer. *Boundary-Layer Meteorol* 118:247–272
- Cheng GD, Li X, Zhao WZ, Xu ZM, Feng Q, Xiao SC, Xiao HL (2014) Integrated study of the water–ecosystem–economy in the Heihe River Basin. *Nat Sci Rev* 1(3):413–428
- Crosman ET, Horel JD (2010) Sea and lake breezes: a review of numerical studies. *Boundary-Layer Meteorol* 137:1–29
- Darbieu C, Lohou F, Lothon M, Vilà-Guerau de Arellano J, Couvreux F, Durand P, Pino D, Patton EG, Nilsson E, Blay-Carreras E, Gioli B (2015) Turbulence vertical structure of the boundary layer during the afternoon transition. *Atmos Chem Phys* 15:10071–10086
- De Roo F, Mauder M (2017) The influence of idealized surface heterogeneity on virtual turbulent flux measurements. *Atmos Chem Phys Discuss*. <https://doi.org/10.5194/acp-2017-498>
- Eder F, De Roo F, Kohner K, Desjardins RL, Schmid HP, Mauder M (2014) Evaluation of two energy balance closure parametrizations. *Boundary-Layer Meteorol* 151:195–219
- Eder F, Schmidt M, Damian T, Traummer K, Mauder M (2015a) Mesoscale eddies affect near-surface turbulent exchange: evidence from lidar and tower measurements. *J Appl Meteorol* 54:189–206
- Eder F, De Roo F, Rotenberg E, Yakir D, Schmid HP, Mauder M (2015b) Secondary circulations at a solitary forest surrounded by semi-arid shrubland and their impact on eddy-covariance measurements. *Agric For Meteorol* 211–212:115–127
- Finnigan JJ (2000) Turbulence in plant canopies. *Annu Rev Fluid Mech* 32:519–571
- Finnigan JJ, Clement R, Malhi Y, Leuning R, Cleugh H (2003) A re-evaluation of long-term flux measurement techniques part I: averaging and coordinate rotation. *Boundary-Layer Meteorol* 107:1–48
- Foken T (2008) The energy balance closure problem: an overview. *Ecol Appl* 18:1351–1367
- Foken T, Wimmer F, Mauder M, Thomas C, Liebethal C (2006) Some aspects of the energy balance closure problem. *Atmos Chem Phys* 6:4395–4402
- Foken T, Aubinet M, Finnigan JJ, Leclerc MY, Mauder M, Paw UKT (2011) Results of a panel discussion about the energy balance closure correction for trace gases. *Bull Am Meteorol Soc* 92(4):ES13–ES18
- Gao ZQ, Horton R, Liu HP (2010) Impact of wave phase difference between soil surface heat flux and soil surface temperature on soil surface energy balance closure. *J Geophys Res* 115:D16112. <https://doi.org/10.1029/2009JD013278>
- Gao ZM, Liu HP, Katul GK, Foken T (2017) Non-closure of the surface energy balance explained by phase difference between vertical velocity and scalars of large atmospheric eddies. *Environ Res Lett* 12(3):034025
- Goulart A, Degrazia G, Rizza U, Anfossi D (2003) A theoretical model for the study of convective turbulence decay and comparison with large-eddy simulation data. *Boundary-Layer Meteorol* 107:143–155
- He Y, Monahan AH, McFarlane NA (2013) Diurnal variations of land surface wind speed probability distributions under clear-sky and low-cloud conditions. *Geophys Res Lett* 40:3308–3314
- Huang J, Lee X, Patton EG (2008) A modelling study of flux imbalance and the influence of entrainment in the convective boundary layer. *Boundary-Layer Meteorol* 127(2):273–292
- Inagaki A, Letzel MO, Raasch S, Kanda M (2006) Impact of surface heterogeneity on energy imbalance: a study using LES. *J Meteorol Soc Jpn* 84:187–198
- Kanda M, Inagaki A, Letzel MO, Raasch S, Watanabe T (2004) LES study of the energy imbalance problem with eddy covariance fluxes. *Boundary-Layer Meteorol* 110:381–404
- Kristensen L, Mann J, Oncley SP, Wyngaard JC (1997) How close is close enough when measuring scalar fluxes with displaced sensors. *J Atmos Ocean Technol* 14:814–821
- Lee X (1998) On micrometeorological observations of surface-air exchange over tall vegetation. *Agric For Meteorol* 91:39–49
- Leuning R, van Gorsel E, Massman WJ, Isaac PR (2012) Reflections on the surface energy imbalance problem. *Agric For Meteorol* 156:65–74
- Li X, Cheng GD, Liu SM, Xiao Q, Ma MG, Jin R, Che T, Liu QH, Wang WZ, Qi Y, Wen JG, Li HY, Zhu GF, Guo JW, Ran YH, Wang SG, Zhu ZL, Zhou J, Hu XL, Xu ZW (2013) Heihe Watershed Allied Telemetry Experimental Research (HiWATER): scientific objectives and experimental design. *Bull Am Meteorol Soc* 94:1145–1160
- Li X, Yang K, Zhou YZ (2016) Progress in the study of oasis-desert interactions. *Agric For Meteorol* 230–231:1–7

- Liu SM, Xu ZW, Song LS, Zhao QY, Ge Y, Xu TR, Ma YF, Zhu ZL, Jia ZZ, Zhang F (2016) Upscaling evapotranspiration measurements from multi-site to the satellite pixel scale over heterogeneous land surfaces. *Agric For Meteorol* 230–231:97–113
- Mahrt L (1998) Flux sampling errors for aircraft and towers. *J Atmos Ocean Technol* 15:416–429
- Mahrt L (2010) Computing turbulent fluxes near the surface: needed improvements. *Agric For Meteorol* 150(4):501–509
- Moeng C, Dudhia J, Klemp J, Sullivan P (2007) Examining two-way grid nesting for large eddy simulation of the PBL using the WRF model. *Mon Weather Rev* 135(6):2295–2311
- Nadeau DF, Pardyjak ER, Higgins CW, Fernando HJS, Parlange MB (2011) A simple model for the afternoon and early evening decay of convective turbulence over different land surfaces. *Boundary-Layer Meteorol* 141:301–324
- Oncley SP, Foken T, Vogt R, Kohsiek W, DeBruin HAR, Bernhofer C, Christen A, van Gorsel E, Grantz D, Feigenwinter C, Lehner I, Liebethal C, Liu H, Mauder M, Pitacco A, Ribeiro L, Weidinger T (2007) The energy balance experiment EBEX-2000. Part I: overview and energy balance. *Boundary-Layer Meteorol* 123:1–28
- Patton E, Sullivan P, Moeng C (2005) The influence of idealized heterogeneity on wet and dry planetary boundary layers coupled to the land surface. *J Atmos Sci* 62:2078–2097
- Pino D, Jonker H, Vilà-Guerau De Arellano J, Dosio A (2006) Role of shear and the inversion strength during sunset turbulence over land: characteristic length scales. *Boundary-Layer Meteorol* 121:537–556
- Rannik U, Vesala T (1999) Autoregressive filtering versus linear detrending in estimation of fluxes by the eddy covariance method. *Boundary-Layer Meteorol* 91(2):259–280
- Raupach MR, Shaw RH (1982) Averaging procedures for flow within vegetation canopies. *Boundary-Layer Meteorol* 22:79–90
- Rizza U, Miglietta M, Degrazia G, Acevedo O, Marques Filho E (2013) Sunset decay of the convective turbulence with large-eddy simulation under realistic conditions. *Phys A* 392:4481–4490
- Schalkwijk J, Jonker HJJ, Siebesma AP (2016) An investigation of the eddy-covariance flux imbalance in a year-long large-eddy simulation of the weather at Cabauw. *Boundary-Layer Meteorol* 160:17–39
- Sorbjan Z (1997) Decay of convective turbulence revisited. *Boundary-Layer Meteorol* 82:501–515
- Steinfeld G, Letzel M, Raasch S, Kanda M, Inagaki A (2007) Spatial representativeness of single tower measurements and the imbalance problem with eddy-covariance fluxes: results of a large-eddy simulation study. *Boundary-Layer Meteorol* 123:77–98
- Stoy PC, Mauder M, Foken T, Marcolla B, Boegh E, Ibrom A, Arain MA, Arneth A, Aurela M, Bernhofer C, Cescatti A, Dellwik E, Duce P, Gianelle D, van Gorsel E, Kiely G, Knohl A, Margolis H, McCaughey H, Merbold L, Montagnani L, Papale D, Reichstein M, Saunders M, Serrano-Ortiz P, Sottocornola M, Spano D, Vaccari F, Varlagin A (2013) A data-driven analysis of energy balance closure across FLUXNET research sites: the role of landscape scale heterogeneity. *Agric For Meteorol* 171–172:137–152
- Talbot C, Bou-Zeid E, Smith J (2012) Nested mesoscale large-eddy simulations with WRF: performance in real test cases. *J Hydrometeorol* 13(5):1421–1441
- Twine TE, Kustas WP, Norman JM, Cook DR, Houser PR, Meyers TP, Prueger JH, Starks PJ, Wesely ML (2000) Correcting eddy-covariance flux underestimates over a grassland. *Agric For Meteorol* 103:279–300
- Wang JM, Wang WZ, Liu SM, Ma MG, Li X (2009) The problems of surface energy balance closure: an overview and case study. *Adv Earth Sci* 24:705–713 (in Chinese)
- Wilson K, Goldstein A, Falge E, Aubinet M, Baldocchi D, Berbigier P, Bernhofer C, Ceulemans R, Dolman H, Field C, Grelle A, Ibrom A, Law BE, Kowalski A, Meyers T, Moncrieff J, Monson R, Oechel W, Tenhunen J, Valentini R, Verma S (2002) Energy balance closure at FLUXNET sites. *Agric For Meteorol* 113:223–243
- Wohlfahrt G, Widmoser P (2013) Can an energy balance model provides additional constraints on how to close the energy imbalance? *Agric For Meteorol* 169:85–91
- Xu ZW, Liu SM, Li X, Shi SJ, Wang JM, Zhu ZL, Xu TR, Wang WZ, Ma MG (2013) Intercomparison of surface energy flux measurement systems used during the HiWATER-MUSOEXE. *J Geophys Res Atmos* 118:13140–13157
- Xu ZW, Ma YF, Liu SM, Shi WJ, Wang JM (2017) Assessment of the energy balance closure under advective conditions and its impact using remote sensing data. *J Appl Meteorol* 56(1):127–140
- Zhang N, Wang XY, Peng Z (2014) Large-eddy simulation of mesoscale circulations forced by inhomogeneous urban heat island. *Boundary-Layer Meteorol* 151(1):179–194
- Zhu X, Ni G, Cong Z, Sun T, Li D (2016) Impacts of surface heterogeneity on dry planetary boundary layers in an urban-rural setting. *J Geophys Res Atmos* 121:12164–121179